Electrochemical conversion of CO_2 into formic acid on TiVC MXenes: A Computational prediction

Kamal Kumar[1#], Archana Singh Kharb[1#], Nora H. de Leeuw[2,3], Jost Adam[4,5], Abhishek K. Mishra[1,*]

[1]Department of Physics, Applied Science Cluster, School of Advanced Engineering, UPES, Dehradun, Uttarakhand 248007, India

[2]Department of Chemistry, University of Leeds, Leeds LS2 9JT, UK

[3]Department of Earth Sciences, Utrecht University, 3584 CB Utrecht, The Netherlands

[4]Computational Materials and Photonics, Department of Electrical Engineering and Computer Science (FB 16) and Institute of Physics (FB 10), University of Kassel, Wilhelmshoher Allee 71, 34121 Kassel, Germany

[5]Center for Interdisciplinary Nanostructure Science and Technology, University of Kassel, Heinrich-Plett-Straße 40, 34132 Kassel, Germany

* Corresponding author email: akmishra@ddn.upes.ac.in (AKM), # equal contributions

Abstract

MXenes are a rapidly growing family of two-dimensional (2D) nanomaterials distinguished by their remarkable catalytic activity and large surface area. TiVC is a recently synthesized M_2C-type MXene composed of titanium, vanadium, and carbon atoms. In this study, we have investigated CO_2 adsorption on pristine and surface-functionalized (O, Cl, F, S, and OH) configurations of ordered TiVC (O-TiVC) and solid solutions (S-TiVC). Our study reveals that both O-TiVC and S-TiVC MXenes effectively activate CO_2 for its catalytic conversion, with maximum adsorption energies of -363.3 kJ/mol and -296.5 kJ/mol, respectively. Additionally, both configurations are found to dissociate the CO_2 molecule spontaneously upon contact. After functionalization of TiVC (by -O, -Cl, -F, and -S), the strong chemisorption of CO_2 turns into weak physisorption, whereas -OH functionalization of both O-TiVC and S-TiVC MXenes results in the conversion of the CO_2 molecule into a formate ($HCOO^-$) ion intermediate. Furthermore, the co-adsorption of this formed HCOO- and an H atom led to formic acid (HCOOH) formation on both -OH functionalized O-TiVC and S-TiVC surfaces. Thus, in our study, we found that the formation of formic acid at the surface of -OH functionalized TiVC MXene efficiently bypasses the major thermodynamic barrier associated with multi-step CO_2 hydrogenation steps.

Keywords: TiVC MXene, DFT, Electrochemical CO_2 Conversion

1. Introduction

The rapid increase in the concentration of carbon dioxide (CO_2) in the Earth's atmosphere, primarily due to the excessive burning of fossil fuels (e.g., oil and coal), is responsible for global warming and climate change [1]. The extra CO_2 emitted into the atmosphere acts as a blanket, trapping the sun's heat and making the Earth's surface warmer [2]. This trapping leads to ocean acidification, the melting of glaciers and mountain ice, increased sea levels, and unpredictable weather events [3]. The catalytic conversion of CO_2 into value-added products is an attractive approach to address these problems [4-10].

Various materials have been proposed to optimize the efficiency of CO_2 capture and conversion [11,12]. Still, the performance of many traditional materials is sub-optimal due to their limited capability to adsorb and reduce CO_2, especially in harsh operating environments [13-17]. The recent progress and emergence of two-dimensional (2D) materials [18], such as graphene, have introduced new possibilities for the development of highly efficient catalysts [19]. In contrast to conventional adsorbent materials, the high surface-to-bulk ratio of 2D materials means that a large proportion of the material is exposed for chemical reactions [20]. This unique property of 2D materials is highly beneficial for their applications in catalysis [21]. In the quest to explore alternatives to conventional adsorbent materials for CO_2 storage and activation [22], MXenes, a category of 2D materials composed of transition metal nitrides, carbides, and carbonitrides, provide a viable solution owing to their ability to effectively adsorb gas molecules [23-28]. This special class of 2D materials possesses abundant functional groups and a high surface area, providing ample active sites to adhere CO_2 molecules [29,30]. These properties are crucial to capture CO_2 from various sources, including power plants and industrial waste [31]. The high durability and stability of MXenes ensure their sustained and effective CO_2 storage capabilities across diverse environmental conditions [32,33]. As a result of their novel properties, pristine and functionalized MXenes are explored for various applications, including gas sensing, energy storage, and catalysis [34,35].

MXenes have the general chemical formula $M_{n+1}X_nT_x$, where M denotes an early transition metal, X represents either nitrogen or carbon, and n ranges from 1 to 3 and defines the width of the MXene [36]. T_x represents one of the most general terminations (or functionalizations), such as F (fluorine), O (oxygen), H (hydrogen), S (sulfur), or OH (hydroxyl group), which are integral to the

synthesis process [36]. Over 25 distinct 2D MXenes have already been synthesized using hydrogen fluoride from the MAX phase precursor, derived from at least three (M_2X, M_3X_2, and M_4X_3) stoichiometries [37]. The symbol A in the MAX phase denotes p-block elements like aluminum (Al) and silicon (Si) [36,37]. A significant body of literature supports the suitability of M_2C MXene in catalysis and gas adsorption [39,40]. Huang *et al*. [39] employed calculations based on the density functional theory (DFT) to explore the CO_2 capture and reduction ability of nine M_2C-type MXenes (where M = Cr, Ti, Zr, V, Hf, Nb, W, Ta, Mo) [39]. They reported an effective adsorption as well as activation of the CO_2 molecule on all nine types of MXene [39]. Among all considered MXenes, Cr_2C and V_2C MXenes exhibited excellent electrochemical reduction performance, with limiting potentials of -1.28 V and -1.19 V, respectively [39]. The DFT study of Guo *et al*. [40] revealed that M_2C-type MXenes exhibit inherent CO_2 activation abilities, preferring CO_2 over H_2O, and Mo_2C MXene enabled an efficient electrocatalytic reduction of CO_2 to CH_4 [40]. The CO_2 capture ability of MXenes can be enhanced by surface functionalization and the addition of CO_2-philic components [41]. The functional groups attached to the MXene surfaces can interact with CO_2 (or other gas molecules) through various chemical interactions, including electrostatic interactions, hydrogen bonding, and Lewis acid-base interactions [41]. Additionally, surface functionalization can enhance the adsorption sites and promote binding between the MXene and gas molecules [41]. Zhang *et al*. [42] employed first-principles calculations to investigate CO_2 reduction on O-functionalized MXenes, specifically Ti_2CO_2, V_2CO_2, and $Ti_3C_2O_2$ [42]. They found that the Ti_2CO_2 MXene exhibits superior catalytic performance in the photocatalytic reduction of CO_2 to HCOOH, with an energy barrier of just 0.53 eV [42]. Junkaew *et al*. [43] investigated the selectivity and activity of pristine and O-functionalized M_2C (M = Ti, Nb, V, Mo) MXenes towards the adsorption of various gas molecules, including H_2, N_2, NO, CO, CO_2, NO_2, H_2S, SO_2, NH_3 and H_2O [43]. They classified the adsorption of these gas molecules on MXenes as strong chemisorption with low selectivity and high reactivity [43]. In contrast, the O-functionalized MXenes were more selective towards a specific gas than their pristine counterparts [43]. In addition to carbide MXenes, recent DFT studies have demonstrated that nitride MXenes also exhibit favourable CO_2 adsorption and activation properties, underscoring the versatility of MXenes as electrocatalysts for CO_2 conversion [44-47]. These findings suggest that both carbide- and nitride-based MXenes represent promising platforms for tuning catalytic activity through

compositional and surface engineering, motivating further theoretical and experimental investigations [42-47].

Recently, Yazdanparast et al. [48] have reported the successful experimental synthesis of a TiVC MXene solid solution through the chemical etching of the TiVAlC MAX, confirming the presence of various functional groups, including -O, -Cl, -F, and -OH, via EDS and XPS studies [48]. A DFT study by Huang *et al*. [49] has shown that TiVC exhibits faster charge and discharge rates and is therefore a promising candidate for lithium-ion batteries [49]. However, this novel M_2C-type MXene has not yet been explored for catalytic applications [49].

In this work, we have used DFT-based computations to explore and investigate CO_2 activation on pristine and functionalized (by O, Cl, F, S, and OH) TiVC MXenes, both in their ordered (O-TiVC) and solid-solution (S-TiVC) configurations. In particular, we have identified the preferred adsorption sites for CO_2 on O-TiVC and S-TiVC, as well as the conversion through a detailed thermodynamic analysis, accompanied by structural and electronic changes. Unlike previously reported MXene catalysts, the OH-functionalized TiVC surface enables spontaneous and barrierless CO_2 reduction to formate ($HCOO^-$) without the need for an external hydrogen source or applied bias. This behavior originates from the cooperative interaction between mixed-metal Ti-V active sites and surface hydroxyl groups, which effectively stabilize key reaction intermediates. Furthermore, the subsequent hydrogenation of the bound formate species results in the formation of the valuable formic acid product, demonstrating a continuous CO_2 reduction pathway. In realistic electrochemical environments, surface hydrogen can be replenished from the electrolyte, ensuring sustained catalytic activity. These findings establish OH-functionalized TiVC MXene as a promising and energetically favorable catalyst for CO_2-to-formic acid conversion

2. Computational Methodology and Calculation Details

The Quantum Espresso (QE) [50] software package was used to perform the DFT [51] calculations and model structural, electronic and surface properties. The generalized gradient approximation (GGA) [52], along with the Perdew-Burke-Ernzerhof (PBE) [53] exchange-correlation function, were chosen for the description of the electronic correlations, whereas electron-ion interactions were described using ultrasoft pseudopotentials (USPP) [54]. A well-tested kinetic energy cutoff of 52 Ry was chosen for the precise representation of electron states and the expansion of the electronic wavefunction in a plane wave basis set. To capture the electron behaviour throughout

the entire reciprocal space, a 7×7×1 k-point mesh was considered for the sampling of the Brillouin zone. The convergence thresholds for forces and total energy were set to 10^{-3} Ry/Bohr and 10^{-4} Ry, respectively. To avoid interactions between the periodic images of the CO_2 molecule, a 3×3×1 supercell of TiVC MXene was considered, and a vacuum of 15 Å was applied in the z-direction. The Grimme-d3 [55] correction was applied to account for the interaction energy resulting from Van der Waals interactions between the adsorbate (CO_2) and the adsorbent (TiVC).

The cohesive energy (E_c) [56-58] of TiVC and $TiVCT_2$ MXenes was calculated by equation (i):

$$E_C = E_{TiVC/TiVCT2} - (n_1E_{Ti} + n_2E_V + n_3E_C + n_4E_T)/n \quad \text{(i)}$$

where n_1, n_2, n_3, and n_4 are the total number of Ti, V, C, and T atoms, respectively, while n= n_1+ n_2+n_3+n_4. $E_{TiVC/TiVCT2}$ is the total energy of the TiVC/$TiVCT_2$ MXene, and E_{Ti}, E_V, E_C, and E_T are the total energies of the isolated Ti, V, C, and T (=O, Cl, F, S, and OH) atoms, respectively.

The adsorption energy E_{ads} was calculated by equation (ii):

$$E_{ads} = E_{TiVC/TiVCT2+CO2} - (E_{TiVC/TiVCT2} - E_{CO2}) \quad \text{(ii)}$$

where $E_{TiVC/TiVCT2+CO2}$ is the total energy of the TiVC/$TiVCT_2$ systems with adsorbed CO_2, and E_{CO2} is the energy of the isolated CO_2 molecule. The Gibbs free energy of various reaction intermediates is calculated by:

$$\Delta G = E_{ads} + \Delta E_{ZPE} - T\Delta S \quad \text{(iii)}$$

where ΔE_{ZPE}, T, and ΔS are the change in zero-point energy, the temperature, and the change in entropy, respectively.

3. Results and discussion

We first modelled the pristine TiVC (in both O-TiVC and S-TiVC configurations) (**Figure 1**). We investigated the effect of surface functionalization (with O, Cl, F, S, and OH atoms) on the structural and electronic properties of the material. Next, we investigated the interaction of the CO_2 gas molecule with pristine and functionalized O-TiVC and S-TiVC MXenes (**Figure 2**).

3.1 Pristine and functionalized TiVC

The space group of O-TiVC is P3m1 (space group no. 164), and its unit cell contains one titanium (Ti), one vanadium (V), and one carbon (C) atom. The pristine O-TiVC MXene cell is constructed by replacing one V-layer of V_2C MXene with a Ti-layer (**Figure 1(a)**). This change in the crystal structure of V_2C MXene results in a geometry comprising ternary layers in the Ti-C-V sequence, in which one C layer is sandwiched between the Ti and V layers. However, the atomic arrangement of S-TiVC MXene is quite different from that of O-TiVC MXene. In S-TiVC MXenes, V and Ti atoms are distributed alternately in both surfaces compared to O-TiVC, where there are only either Ti or V atoms in each surface (**Figure 1(c)**). The 3×3×1 supercell considered here comprises nine Ti, nine V, and nine C atoms. The relaxed lattice parameters of both O-TiVC and S-TiVC MXenes were found to be 2.96 Å, in agreement with the earlier calculated values of Huang *et al*. [49]. The optimized Ti-C and V-C bond lengths were also found to match well with the literature (**Table 1**). The functionalized $TiVCT_2$ MXenes (T=-O, -Cl, -F, -S, and -OH) were modeled by saturating V and Ti atoms with -O, -Cl, -F, -S, and -OH functional groups. To assess the stability of TiVC and $TiVCT_2$ MXenes, we have calculated E_c through **equation (i)**. The calculated E_c for all O-TiVC and S-TiVC configurations are very similar, suggesting that both ordered and solid-solution MXenes are thermodynamically viable and are expected to co-exist. Solid solution structures are slightly more favorable, and S-TiVC MXenes are typically obtained in experiments. Hence, both models were considered in this study to ensure theoretical completeness and consistency with experimental observations. Among all the studied functionalized MXenes, the O-terminated TiVC MXene (O-$TiVCO_2$) was found to be thermodynamically the most stable system. The calculated E_c for -O, -F, -S, -OH, and -Cl functionalized O-TiVC MXenes are -8.41, -7.37, -7.18, -6.96, and -6.49 eV, respectively, confirming the higher stability of the O surface termination. The optimized bond lengths (Å) and E_c (eV) of the pristine and functionalized TiVC MXenes are given in **Table 1,** and the relaxed geometries of all O-$TiVCT_2$ and S-$TiVCT_2$ derivatives are shown in **Figures S1** and **S2** of the supplementary information (SI). Similar to O-$TiVCT_2$, different functionalized derivatives of S-$TiVCT_2$ were also found to be thermodynamically favorable, as shown by the calculated negative E_c (**Table 1**).

To understand the electronic properties of O-TiVC and S-TiVC MXenes, the projected densities of states (PDOS) were plotted in **Figures 1(c)** and **1(d)**. The PDOS reveal that both O-TiVC and S-TiVC possess metallic character, which is preserved after surface functionalization to O-$TiVCT_2$ and S-$TiVCT_2$ (**Figures S3** and **S4**).

Table 1

Optimized bond lengths (Å) and cohesive energies (eV) of pristine and functionalized TiVC MXene

	T	E_c	Ti-C		V-C	Ti-T	V-T	O-H
			Our work	Huang *et al.* [49]				
O-TiVC	**----**	-7.75	2.10	--	1.99	--	--	--
	-O	-8.41	2.12	2.15	1.99	1.93	1.89	--
	-Cl	-6.49	2.06	--	2.01	2.45	2.42	--
	-F	-7.37	2.06	2.06	2.01	2.13	2.14	--
	-S	-7.18	2.10	--	2.06	2.38	2.33	--
	-OH	-6.96	2.07	2.06	2.01	2.14	2.13	0.97
S-TiVC	**----**	-7.76	2.09	--	1.99	--	--	--
	-O	-8.43	2.21	2.24	2.01	1.96	2.00	--
	-Cl	-6.49	2.07	--	2.00	2.40	2.45	--
	-F	-7.38	2.07	2.08	2.00	2.12	2.16	--
	-S	-7.19	2.11	--	2.05	2.36	2.35	--
	-OH	-6.97	2.08	2.09	2.00	2.13	2.16	0.97

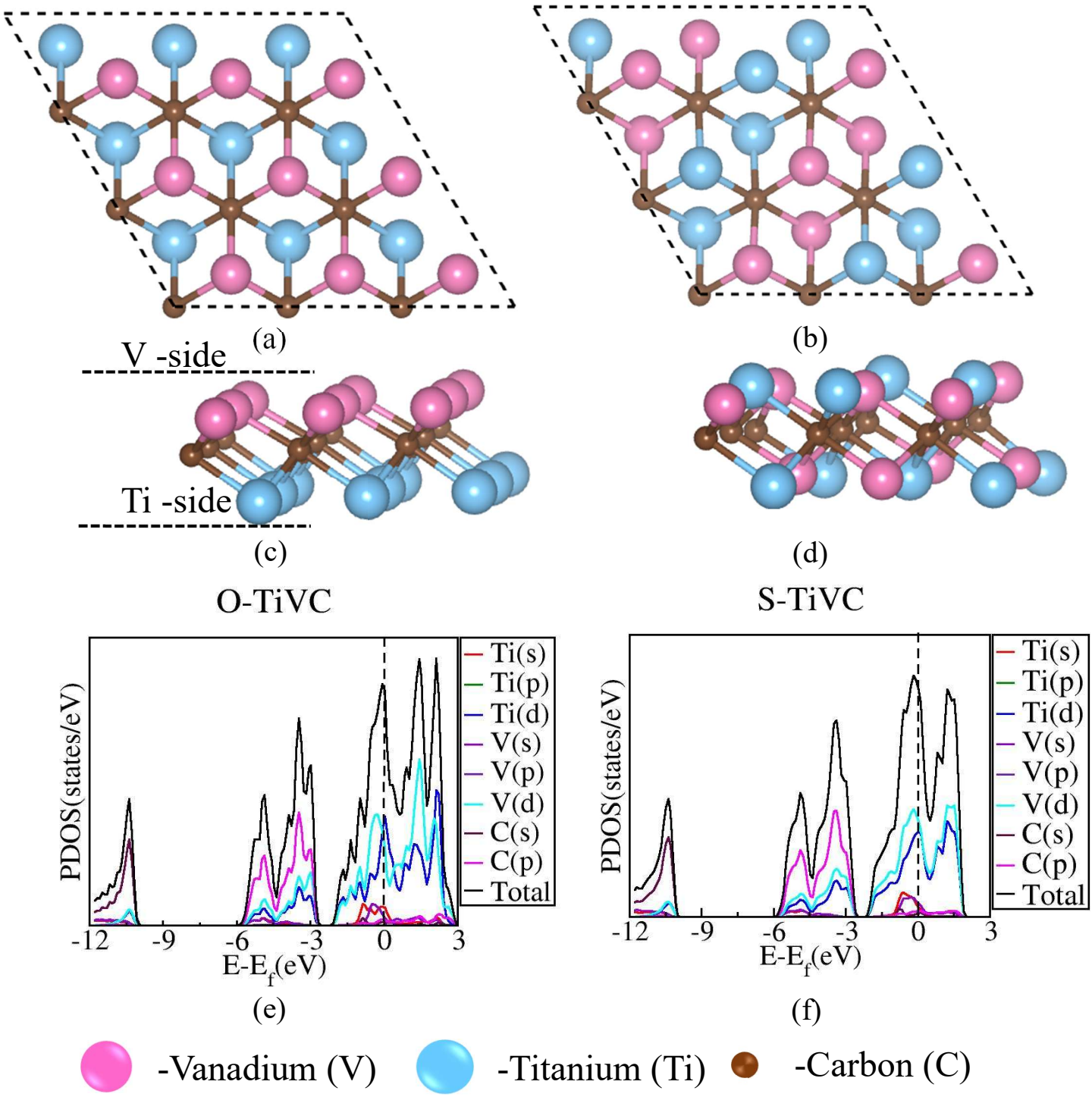

Fig. 1. (a) O-TiVC and (b) S-TiVC top view, (c) O-TiVC and (d) S-TiVC side view. Projected densities of states (PDOS) of O-TiVC (e) and S-TiVC (f). The Fermi level (E_f) was set at zero and shown by a dotted line. TiVC MXene exhibits metallic character in both O-TiVC and S-TiVC configurations. The pink, sky blue, and brown spheres represent vanadium (V), titanium (Ti), and carbon (C) atoms, respectively.

3.2 CO_2 Adsorption/Activation

(a) O-TiVC

As O-TiVC exhibits two distinct surfaces, namely the Ti side and the V side (**Figure 1**), the active sites of both surfaces were assessed for CO_2 adsorption. These sites are above the C and V atoms on the V-side and above the C and Ti atoms on the Ti-side. We have studied various vertical, horizontal, and tilted alignments of the CO_2 molecule at these sites, although here we will discuss only the top eight configurations. After relaxation, we found that when a linear CO_2 molecule is placed horizontally at these sites, it bends and becomes activated for further conversion in four configurations. In contrast, in initially vertical configurations, the adsorption of CO_2 at pristine O-TiVC falls into the category of weak physisorption. The highest E_{ads} (-363.27 kJ/mol) was found for the configuration in which a linear CO_2 molecule was placed above the C atom at the V side and parallel to the surface of O-TiVC MXene (**Figure 2(a)**). In this configuration, CO_2 undergoes structural changes, where its linear geometry is lost as it bends to a bond angle of 115.8°, and the C=O bond elongates to 1.37 Å. These changes confirm the activation of CO_2 at the surface of O-TiVC MXene. During the interaction, the CO_2 molecule acts as an electron acceptor, and a charge transfer of -1.66 e takes place between CO_2 and the O-TiVC MXene. The most favorable position and strong interaction of CO_2 on the V side is also confirmed by the PDOS (**Figure 2(a))**, where the s- and p-orbital peaks of the O atom of the CO_2 molecule coincide with the peak of the d-orbital of the V atom of O-TiVC near -10 eV in the valence band (VB). The major contribution to the valence band arises from the d-orbitals of the Ti and V atoms, and the C atom p-orbitals.

On the Ti side, the highest E_{ads} (-337.94 kJ/mol) is also found when a linear CO_2 molecule is placed horizontally above the C atom (**Figure 2(b)**). In this case, CO_2 adsorbs chemically at an adsorption height of 1.23 Å. The reduction of the CO_2 molecule occurs through a Bader charge transfer of -1.90 e^-. The optimized C-O bond length and bond angle of CO_2 are 1.39 and 114.9°, respectively. Thus, activation of the CO_2 takes place on both surfaces (Ti side and V side) of pristine O-TiVC. The E_{ads} of the other activated CO_2 molecules at O-TiVC are -202.87 kJ/mol (above the V atom at the V side) and -231.47 kJ/mol (above the Ti atom at the Ti side). The adsorption energies (E_{ads}) and adsorption heights of the CO_2 molecule at each considered adsorption site on the O-TiVC MXene surfaces are summarized in **Table 2**, and the relaxed structure of each configuration is shown in **Figure S5**. The calculated value of E_{ads} in several kilojoules per mole (kJ/mol) indicates the high adsorption capacity of the O-TiVC surfaces. In one configuration, the CO_2 molecule even

dissociates into CO and O species during the adsorption process on pristine O-TiVC, a behavior is discussed in detail in Section 3.3.

We next studied the effect of surface functionalization on the CO_2 adsorption characteristic of O-TiVC. When O atoms saturate O-TiVC, the strong chemisorption of CO_2 transforms into a weak physisorption with E_{ads} of only -20.85 kJ/mol and an adsorption height of 2.80 Å **(Figure S6)**. This weak interaction is reflected in the minimal Bader charge transfer (**Figure S7**), which amounts to just 0.004 e^-. We have presented various relaxed configurations of the CO_2 molecule at the O-$TiVCO_2$ MXene in **Figure S6**.

At the O-$TiVCCl_2$ derivative, the CO_2 molecule also binds weakly with a maximum E_{ads} of -16.98 kJ/mol) when the CO_2 molecule is sited above the Ti atom and parallel to the surface (**Figure S8)** Here, the CO_2 molecule interacts at a higher height of 3.07 Å compared to that in O-$TiVCO_2$. As the Cl atom is less electronegative than an O atom, when the CO_2 molecule interacts with O-$TiVCCl_2$, it gains more Bader charge (0.009 e^-) than when it adsorbs on $TiVCO_2$ (**Figure S7)**. **Figure S8** contains the remaining studied configurations of the CO_2 at O-$TiVCCl_2$ derivatives.

Since F is the most electronegative functional group among all considered groups, CO_2 molecules undergo slight oxidation when interacting with the O-$TiVCF_2$ derivative. The charge transfer magnitude is least (0.0001) between CO_2 and O-$TiVCF_2$, and E_{ads} is also the lowest (-16.14 kJ/mol) among all considered derivatives of O-TiVC. **Figure S9** depicts the optimized vertical and horizontal configurations of CO_2 on the O-$TiVCF_2$ derivative. In both F and Cl derivatives, CO_2 tends to adsorb on the Ti side. Even on O-$TiVCS_2$, the CO_2 molecule finds its preferred adsorption site on the Ti side (**Figure S9**). As S is the most electropositive among all the above-mentioned functional groups, now the CO_2 molecule acts as an electron acceptor and becomes negatively charged with a Bader charge transfer of 0.016 e^- (**Figure S7)**. The top and side views of all studied CO_2 configurations on the O-$TiVCS_2$ surface are plotted in **Figure S10**. The calculated E_{ads} of the CO_2 molecule in this configuration is -18.19 kJ/mol (**Table 2**), which is 1.21 and 2.05 kJ/mol more than that of O-$TiVCCl_2$ and O-$TiVCF_2$, respectively. Thus, the order of E_{ads} on various O-TiVC derivatives is F<Cl<S<O, with weak physisorption in all cases. When a CO_2 molecule interacts with the O-$TiVC(OH)_2$ derivative, it spontaneously converts into a formate ion ($HCOO^-$), which we will discuss in detail in section 3.4. The PDOS of the most favorable CO_2 configurations at various O-$TiVCT_2$ MXenes are plotted in **Figure S11** of the SI. The optimized geometries along

with top and side views of various CO_2 configurations on O-TiVC$(OH)_2$ are given in Figure S12 in the SI.

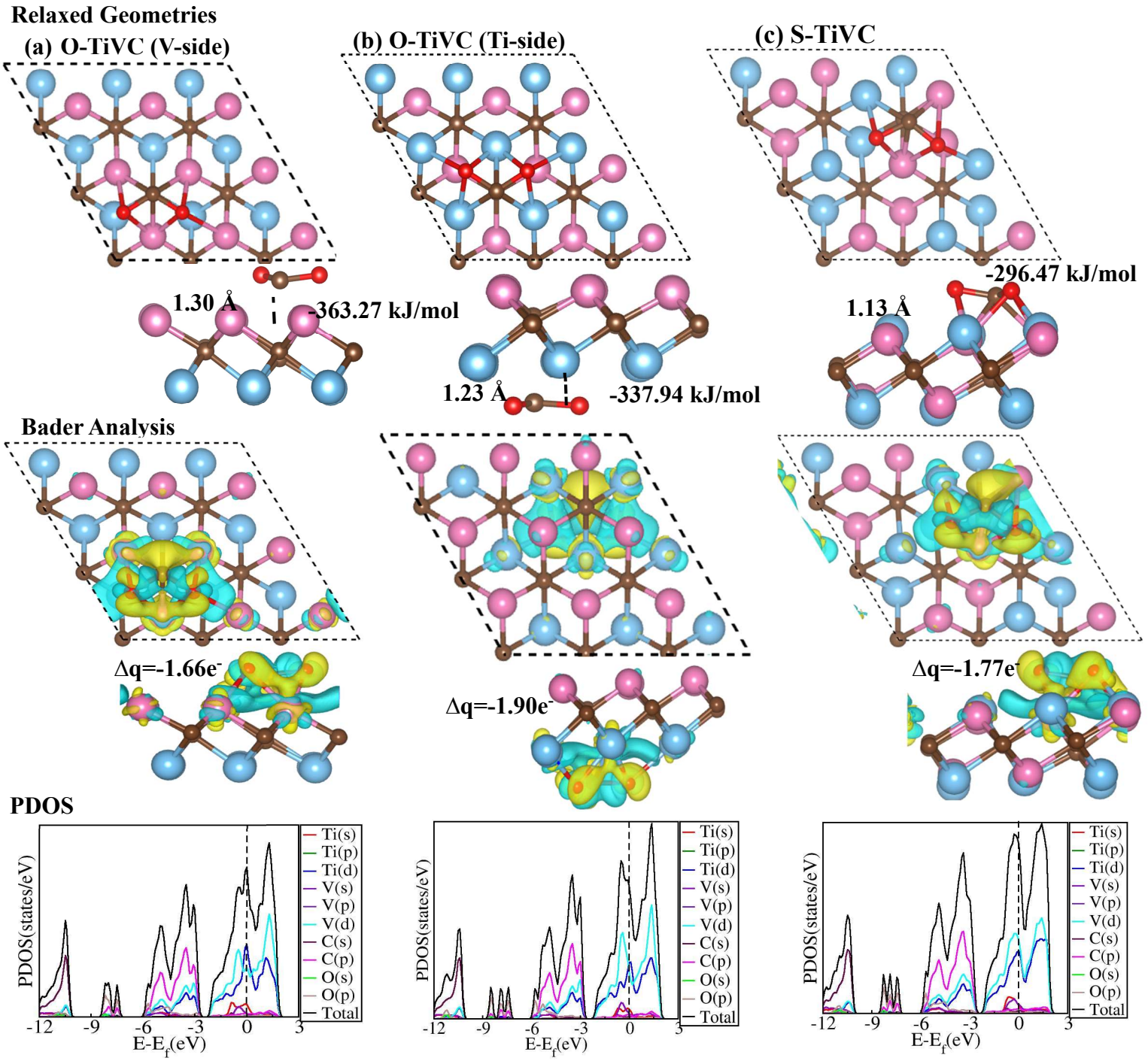

Fig. 2. Optimized structures, charge density difference, and PDOS of the most stable configurations of CO_2 on O-TiVC ((a) V-side, (b) Ti-side) and (c) S-TiVC MXenes. After CO_2 activation, all MXene sheets remain metallic.

Table 2

Calculated adsorption energy E_{ads}(kJ/mol), adsorption height h (Å), C-O bond lengths l(Å), and bond angle θ (°), for various configurations of the CO_2 molecule at TiVC MXene and its functional derivatives.

	Site/Configurations			E_{ads}	h	l	θ
CO_2@O-TiVC	**V-side**	**C**	∥	-363.27	1.31	1.37	115.8°
			⊥	-10.06	3.29	1.17	179.9°
		V	∥	-202.87	1.32	1.36	116.1°
			⊥	-29.89	2.21	1.17	180.0°
	Ti-side	**C**	∥	-337.94	1.23	1.39	114.9°
			⊥	-222.63	---	---	---
		Ti	∥	-231.47	1.22	1.49	105.1°
			⊥	-24.97	2.35	1.19	180.0°
CO_2@O-TiVCO_2	**V-side**	**O**	∥	-20.83	2.84	1.17	179.6°
			⊥	-9.70	3.01	1.17	179.9°
		V	∥	-20.85	2.80	1.17	179.7°
			⊥	-11.48	2.74	1.17	179.9°
	Ti-side	**O**	∥	-17.78	2.91	1.17	179.5°
			⊥	-9.83	3.04	1.17	179.9°
		Ti	∥	-11.58	2.94	1.17	179.8°
			⊥	-19.63	2.75	1.17	180.0°
CO_2@O-TiVCF_2	**V-side**	**F**	∥	-15.54	2.82	1.17	179.4°
			⊥	-8.74	2.95	1.17	179.9°
		V	∥	-15.87	2.76	1.17	179.5°
			⊥	-10.61	2.59	1.17	180.0°
	Ti-side	**F**	∥	-15.79	2.81	1.17	179.9°
			⊥	-8.94	2.96	1.17	180.0°

CO_2@O-TiVCCl$_2$	V-side	Ti	∥	-16.14	2.79	1.17	179.6°
			⊥	-10.86	2.63	1.17	180.0°
		Cl	∥	-16.81	3.27	1.17	179.9°
			⊥	-15.35	3.59	1.17	180.0°
		V	∥	-16.68	3.26	1.17	179.8°
			⊥	-15.31	3.27	1.17	180.0°
	Ti-side	Cl	∥	-16.98	3.27	1.17	179.9°
			⊥	-15.30	3.58	1.17	180.0°
		Ti	∥	-16.02	3.07	1.17	179.9°
			⊥	-15.32	3.22	1.17	179.9°
CO_2@O-TiVCS$_2$	V-side	S	∥	-17.79	3.34	1.17	179.9°
			⊥	-15.89	3.52	1.17	180.0°
		V	∥	-17.95	3.30	1.17	180.0°
			⊥	-16.03	3.32	1.17	180.0°
	Ti-side	S	∥	-17.96	3.34	1.17	179.2°
			⊥	-16.07	3.65	1.18	179.9°
		Ti	∥	-18.19	3.29	1.17	179.6°
			⊥	-16.00	3.42	1.17	180.0°
CO_2@O-TiVC(OH)$_2$	V-side	H	∥	--	--	--	--
			⊥	-25.51	2.31	1.18	180.0°
		V	∥	--	--	--	--
			⊥	-27.05	2.01	1.18	180.0°
	Ti-side	H	∥	--	--	--	--
			⊥	-26.80	2.21	1.17	179.8°
		Ti	∥	-59.85	1.43	1.26	128.6°
			⊥	-28.62	1.92	1.18	179.9°

(b) S-TiVC

Similar to O-TiVC, we considered various adsorption sites of S-TiVC MXene to investigate the interaction of CO_2 molecules. Since both sides of our model of S-TiVC MXene are identical (containing both Ti and V atoms), we have studied CO_2 adsorption at different sites of only one

side of S-TiVC and S-TiVCT_2 MXenes. The most stable configuration of the CO_2 molecule at S-TiVC is shown in **Figure 2 (c)**, where the CO_2 molecule was initially placed parallel to the S-TiVC above the C atom. In this configuration, the E_{ads} of CO_2 is -296.5 kJ/mol (**Table 3**). Similar to the functionalization of O-TiVC, the functionalization of S-TiVC transforms the strong chemisorption into weak physisorption of CO_2. The E_{ads} of the most stable configurations of CO_2 at S-TiVCO_2, S-TiVCCl_2, S-TiVCF_2, and S-TiVCS_2 are calculated to be -19.75, -15.53, -16.92, and -17.95 kJ/mol, respectively (**Table 3**). In all derivatives, the CO_2 molecule remains almost linear, and the C-O bond length remains at 1.17 Å, indicating a physical and exothermic interaction.

In addition to the electronic effects of the surface functional groups and their effect on the surface reactivity, the transformation of strong chemisorption of CO_2 into physisorption at the functionalized surfaces is also due to the steric hindrance caused by the functional groups present on the surface of the MXenes. When O-TiVC and S-TiVC are saturated with different functional groups (=-O, -Cl, -F, -S, and -OH), the functionalized atoms are arranged quite closely to each other, and these closely arranged surface atoms prevent the chemical interaction of CO_2 with O-TiVC and S-TiVC. Furthermore, the functional groups selected for the saturation of TiVC are bulky, having a larger atomic size, which blocks the approach of CO_2 to the TiVC surface. The presence of these functionalization atoms also reduces the exposed surface and adsorption sites available for CO_2 adsorption by occupying those sites that were previously available for interaction with the CO_2 molecule, which increases the distance between CO_2 and the TiVC surface, resulting in low E_{ads} and a weak interaction. As such, the functional groups create steric hindrance, but they also alter the distribution of atomic orbitals in PDOS by either withdrawing or donating electrons to TiVC, which prevents the formation of chemical bonds between TiVC and the CO_2 molecule.

The relaxed geometries of all investigated vertical and horizontal configurations of CO_2 at the pristine and all S-TiVC derivatives are shown in **Figure S13** (at S-TiVC), **S14** (at S-TiVCO_2), **S15** (at S-TiVF_2), **S16** (at S-TiVCF_2), and **S17** (at S-TiVCS_2). **Table 3** contains the E_{ads} value and geometrical parameters. From **Figures S11** and **S18**, it is clear that when O-TiVC and S-TiVC are both functionalized with any functional groups, the highest contribution in the conduction band (CB) of PDOS after CO_2 adsorption arises from the p-orbital of the functional group. Additionally, the CB in all PDOS is primarily dominated by the d-orbitals of V and Ti atoms. Similar to O-TiVC

$(OH)_2$, when a linear CO_2 molecule is allowed to interact with the surface of S-TiVC$(OH)_2$, it converts into an $HCOO^-$ ion with a Bader charge transfer of $-0.82e^-$ and an adsorption height of 1.56 Å. The surface of S-TiVC is found to be too reactive towards CO_2, and in some of the tested configurations, the CO_2 molecule spontaneously dissociated after adsorption, unless it is initially placed in a specific orientation and at a particular position. This dissociation is discussed and explained in section 3(d). **Figure S19** and **S20** of the SI contains the Bader charge transfer and charge density differences of the most stable configurations of CO_2 at the various S-TiVCT_2 surfaces and all studied CO_2 configurations at S-TiVC$(OH)_2$.

Table 3

Calculated adsorption energies E_{ads}(kJ/mol), adsorption heights h (Å), C-O bond lengths l(Å), and bond angles θ (°) for the various configurations of the CO_2 molecule at TiVC MXene and its functional derivatives.

	Site/Configurations		E_{ads}	h	l	θ
CO_2@S-TiVC	**C**	∥	-296.47	1.39	1.38	114.5°
		⊥	-276.86	1.40	1.40	115.0°
	V	∥	-500.56	-	-	-
		⊥	-24.11	2.22	1.18	179.8°
	Ti	∥	-167.22	1.34	1.42	108.2°
		⊥	-32.77	2.47	1.18	179.6°
	O	∥	-16.93	2.77	1.17	179.7°
		⊥	-9.92	2.97	1.17	179.9°
CO_2@S-TiVCO_2	**V**	∥	-19.75	2.74	1.17	179.5°
		⊥	-11.33	2.72	1.17	179.9°
	Ti	∥	-14.74	2.92	1.17	179.7°
		⊥	-12.30	2.67	1.17	180.0°
	F	∥	-15.17	2.73	1.17	179.6°
		⊥	-8.94	2.93	1.17	179.9°
	V	∥	-16.92	2.63	1.17	179.6°

CO_2@S-TiVCF$_2$		⊥	-10.03	2.58	1.17	179.9°
	Ti	∥	-14.83	2.80	1.17	179.8°
		⊥	-11.61	2.53	1.17	179.9°
	Cl	∥	-16.53	2.73	1.17	180.0°
		⊥	-15.49	2.91	1.17	179.9°
CO_2@S-TiVCCl$_2$	**V**	∥	-15.66	2.63	1.17	179.9°
		⊥	-14.99	2.58	1.17	179.9°
	Ti	∥	-15.45	2.79	1.17	179.8°
		⊥	-15.54	2.53	1.17	180.0°
	S	∥	-17.65	3.38	1.17	179.5°
		⊥	-15.93	3.68	1.17	180.0°
CO_2@S-TiVCS$_2$	**V**	∥	-17.63	3.25	1.17	179.7°
		⊥	-16.08	3.36	1.17	180.0°
	Ti	∥	-17.26	3.17	1.17	179.8°
		⊥	-15.83	3.20	1.17	179.8°
	H	∥	-81.90	-	-	-
		⊥	-26.23	2.22	1.17	179.5°
CO_2@STiVC(OH)$_2$	**V**	∥	-64.00	1.23	1.28	123.8°
		⊥	-	-	-	-
	Ti	∥	-5.27	0.63	1.28	124.3°
		⊥	-26.61	1.90	1.18	178.8°

3.3 Dissociation

(a) O-TiVC

As mentioned in earlier sections, in one configuration at the pristine O-TiVC, the CO_2 molecule spontaneously dissociates into CO and O fragments with E_{ads} of -222.63 kJ/mol (**Figure 3(a)**. Such behavior is observed when a linear CO_2 molecule is placed perpendicular to the Ti side of the O-TiVC surface above the C atom, followed by structural relaxation. The dissociated O atom binds with the surface of O-TiVC and forms a stable surface-oxygen species. In contrast, the dissociated CO fragment moves far away from the O-TiVC surface and stabilizes itself at a distance of 3.48

Å, indicating partial dissociation and weak adsorption of the CO molecule. While the surface of O-TiVC is highly reactive and capable of splitting CO_2 molecules, it exhibits a low affinity towards CO, allowing for its facile desorption. Such dissociation is relevant in CO generation applications, but due to the weak interaction, it may restrict further surface-mediated transitions unless additional reaction steps and surface modifications are employed to stabilize and utilize the CO intermediate. After dissociation, -0.02 and -1.22 e^- Bader charge is transferred to the dissociated CO and O fragments, and the net Bader charge on the dissociated CO_2 molecule is -1.23e^- (**Figure 3(a)**). The optimized C≡O bond length of the CO molecule at O-TiVC is 1.13 Å.

(b) S-TiVC

Similar dissociative behavior of the linear CO_2 molecule is found at the surface of the pristine S-TiVC MXene surface when the CO_2 molecule is placed horizontally above a V atom in the S-TiVC surface (**Figure 3(b)**). Upon relaxation, CO_2 splits into O and CO species with an E_{ads} of -500.56 kJ/mol. Unlike O-TiVC, however, where the dissociated CO fragment moves away from the surface, the CO fragment adsorbs chemically at the S-TiVC surface, forming a Ti-O bond of length 2.16 Å. In this case, the C≡O bond of the CO fragment elongates to 1.31 Å. After dissociation, both CO and O become negatively charged, with a Bader charge transfer of -1.32e^- and -1.17e^-, respectively, which confirms the substantial charge transfer from S-TiVC to CO_2 and strong stabilization of both fragments. These outcomes highlight the high dual-fragment stabilization ability of pristine S-TiVC MXene. Thus, S-TiVC should be a suitable candidate for multi-step CO_2 electrochemical conversion pathways that depend on both CO retention and further surface reactivity. The strong chemisorption and spontaneous dissociation of CO_2 on the pristine TiVC surface can be attributed to the high reactivity of the exposed Ti and V atoms, which possess unsaturated coordination and high density of available d-states near the Fermi level. These characteristics facilitate strong orbital overlap and charge transfer with the orbitals of the CO_2 molecule, weakening its C=O bonds and favoring dissociation without an external energy barrier.

Dissociation

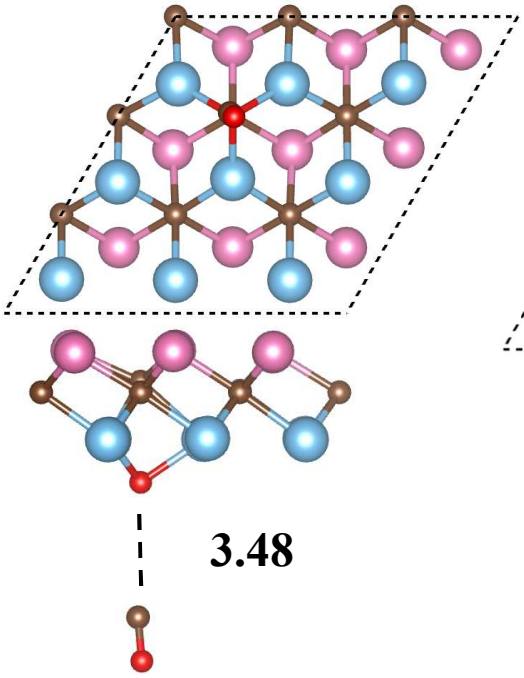

3.48

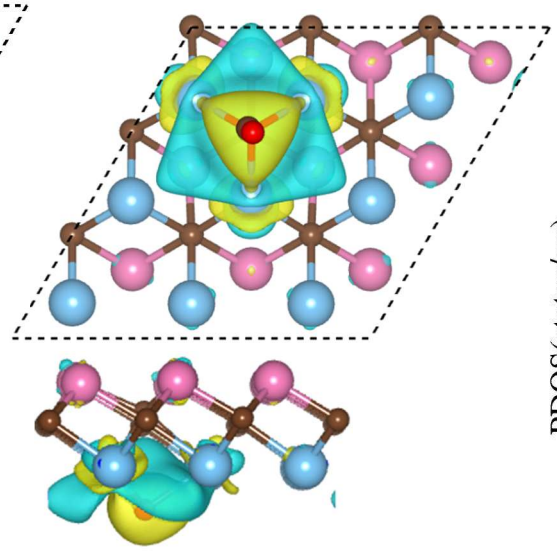

Δq_{co2}= -1.23e$^-$

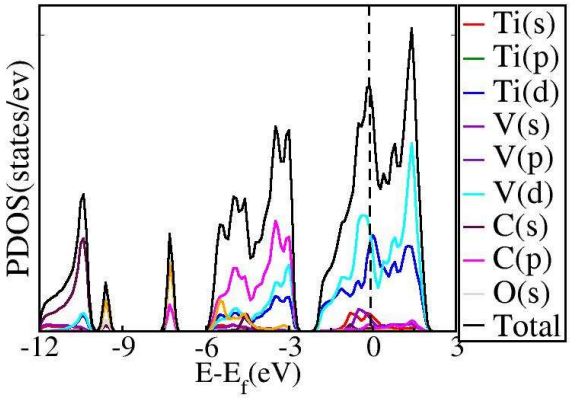

(a)

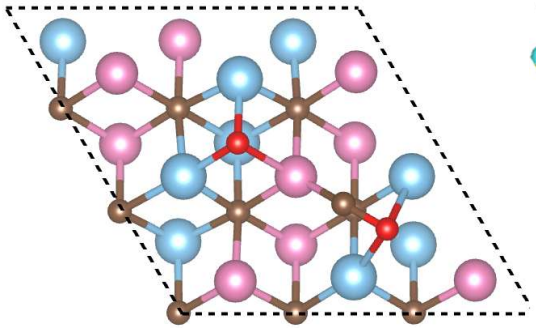

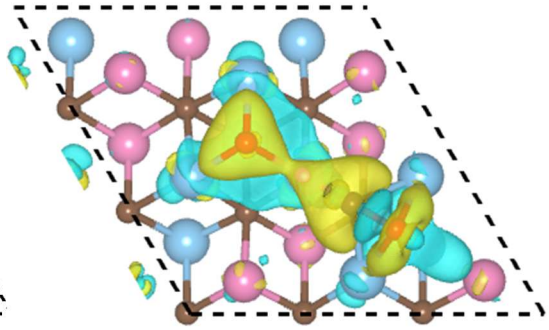

Δq_{co2}= -2.49e$^-$

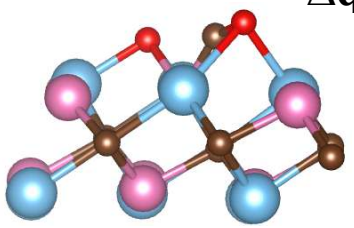

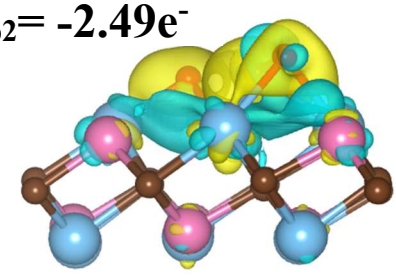

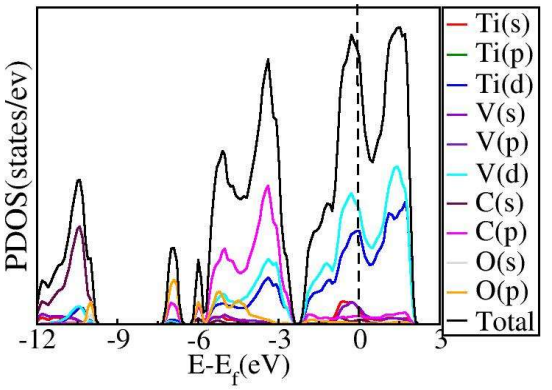

(b)

Fig. 3. Relaxed geometries, charge density difference plots, and PDOS of the CO_2 molecule after dissociation on (a) O-TiVC and (b) S-TiVC MXenes.

3.4 Formate formation

(a) O-TiVC

The CO_2 adsorption on O-TiVC$(OH)_2$ is an interesting case, where an initially linear CO_2 molecule, when it comes into contact with this derivative, spontaneously converts into a formate ion ($HCOO^-$) at an adsorption height of 1.52 Å (**Figure 4**). The anionic character of the formed $HCOO^-$ is validated by the negative Bader charge transfer of $0.82e^-$ onto the $HCOO^-$ ion. The increment in C-O bond length from 1.16 Å to 1.27 Å confirms the breaking of the sp^2 hybridized C=O bond and formation of a new C-H bond of length 1.12 Å. Additionally, the O-C-O bond angle reduces to 128.67°, and the optimized tetrahedral angle is 179.46°, ensuring the planar geometry of the $HCOO^-$ ion. The Gibbs free energy of this step is -250.36 kJ/mol. **Table 4** summarizes the relaxed geometrical parameters of the formed $HCOO^-$ ion. Upon adsorption on O-TiVC$(OH)_2$, the CO_2 molecule undergoes adsorption-induced activation, where hydrogen transfer from a surface -OH group leads to the barrierless formation of a $HCOO^-$ intermediate.

(b) S-TiVC

S-TiVC$(OH)_2$ is also highly reactive towards CO_2 adsorption activation, with the initially linear CO_2 molecule converting into $HCOO^-$ at a height of 1.56 Å, with a Bader charge transfer of $-0.82e^-$ and ΔG of -292.02 kJ/mol. The relaxed structural parameters of the formed $HCOO^-$ are in good agreement with earlier reported theoretical and experimental values (refer to **Table 4**). From the PDOS, it is clear that the strong interaction between CO_2 and OH-terminated MXenes leads to the redistribution of atomic orbitals near the Fermi level. Since the tetrahedral angle (θ_T) of the $HCOO^-$ ion is 179.99°, the geometry of the $HCOO^-$ ion is planar. Thus, both ordered and solid solution configurations of TiVC$(OH)_2$ are suitable for the electrocatalytic reduction of CO_2. Surface functionalization significantly modifies the electronic structure of TiVC MXene by introducing surface dipoles and passivating reactive metal sites. For example, terminations such as O, F, Cl, and S saturate the surface dangling bonds, reducing the availability of active electronic states near the Fermi level, which in turn weakens the interaction with CO_2, leading primarily to physisorption. In contrast, -OH functionalization not only provides hydrogen atoms capable of

interacting with CO_2, but also creates favorable local electronic environments that stabilize the formation of the formate intermediate via hydrogen bonding and charge redistribution. The formation of formate ($HCOO^-$) on -OH functionalized TiVC is facilitated by a synergistic effect of the surface hydroxyl group acting as a proton donor, and the electronically active Ti and V centers promoting electron transfer to the CO_2 molecule. This reduces the energy barrier for the proton-coupled electron transfer step, explaining the selective formation of the formate intermediate over other possible products.

The PDOS analysis shows that V d-states exhibit a higher density near the E_f than Ti(d) states, indicating enhanced electronic activity. The higher density of V(d)states near the E_f provides improved charge-transfer capability, making V sites more active toward CO_2 activation than Ti sites. Strong V(d)-C(p) hybridization further stabilizes the $HCOO^-$ intermediate, leading to reduced free-energy changes in formate formation compared to Ti-based MXenes.

Table 4

Gibbs free energy ΔG (kJ/mol), bond lengths l(Å), and bond angles θ (°) of $HCOO^-$ ion at -OH functionalized O-TiVC and S-TiVC MXenes. The experimental and theoretical values are included for comparison to validate the formation of the $HCOO^-$ reaction intermediate.

MXenes	ΔG	Δq	l			θ			
			l_1(C-O1)	l_1(C-O2)	l_3(C-H)	θ_1	θ_2	θ_3	θ_T
O-TiVC(OH)$_2$	-250.36	-0.82	1.27	1.27	1.12	115.63	115.69	128.67	179.46
S-TiVC(OH)$_2$	-292.02	-0.82	1.28	1.26	1.12	115.87	116.79	127.32	179.99
Experimental [59]	---	---	---	---	---	---	---	126.00	---
Theoretical [60]	---	---	---	1.26	1.14	---	---	130.44	---

Upon CO_2 adsorption on $TiVC(OH)_2$, a hydrogen atom from a surface –OH group is spontaneously transferred to CO_2, leading to the formation of a $HCOO^-$ intermediate. Although this step involves hydrogen donation from surface -OH terminations, it does not imply irreversible surface degradation. Under realistic electrochemical or catalytic conditions, surface -OH groups can be regenerated through proton transfer from the electrolyte or via co-adsorbed hydrogen species, as

reported for OH-terminated MXenes. Therefore, the observed spontaneous formate formation represents an initial CO_2 activation step rather than permanent consumption of surface hydrogen.

The reaction mechanism on $TiVC(OH)_2$ proceeds predominantly via a formate pathway. CO_2 adsorption induces strong interaction with surface metal sites and adjacent -OH groups, resulting in hydrogen transfer from -OH to CO_2 and spontaneous formation of an O-bound $HCOO^-$ intermediate. This configuration is strongly stabilized on the surface, making the formate pathway energetically favourable. Alternative pathways leading to CO formation typically involve a COOH intermediate, which is not stabilized on the $TiVC(OH)_2$ surface owing to weaker C-bound interactions compared to O-bound species. Moreover, hydrogen evolution is suppressed because surface hydrogen preferentially participates in CO_2 activation rather than H-H recombination.

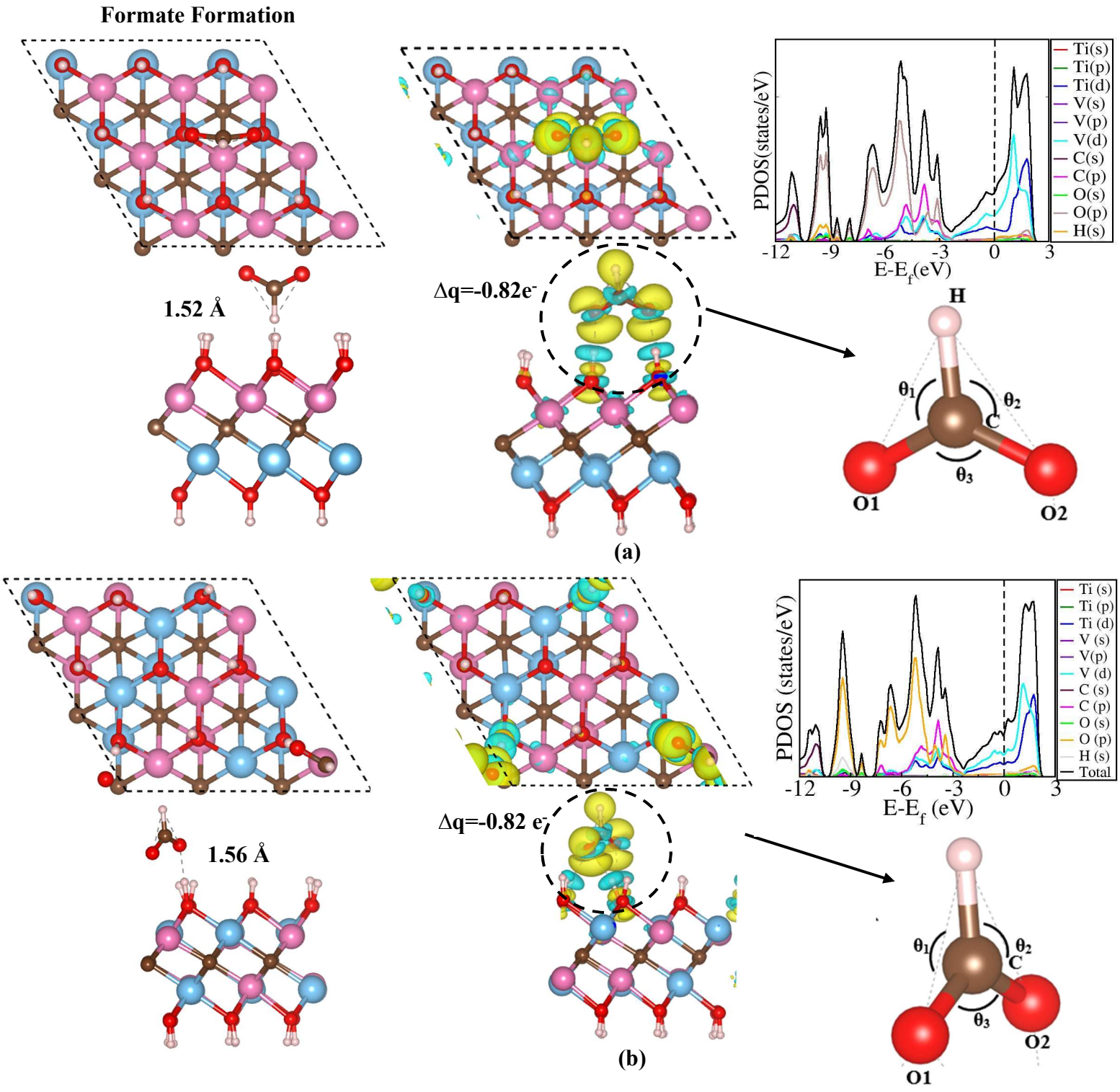

Fig. 4. Relaxed geometries, charge density differences, and PDOS of CO_2 after formate formation at (a) O-TiVC$(OH)_2$ and (b) S-TiVC$(OH)_2$ MXenes.

3.5 Formic acid formation

After the formation of the $HCOO^-$ intermediate, the co-adsorption of $HCOO^-$ and an additional atomic hydrogen is considered to investigate the hydrogenation pathway toward HCOOH formation. The atomic hydrogen does not originate from the remaining surface -OH groups but represents hydrogen supplied from the reaction environment (e.g. proton-electron pairs or co-adsorbed hydrogen), a commonly adopted approach in DFT studies of CO_2 reduction. Similar hydrogen-assisted hydrogenation steps have been reported for OH-terminated MXenes and related systems. While the present calculations focus on individual elementary steps, surface -OH groups are expected to be regenerated under realistic electrochemical conditions through proton transfer from the electrolyte after HCOOH desorption. Although the $CO_2 \rightarrow HCOO^-$ transformation is thermodynamically favourable and occurs without an apparent activation barrier upon adsorption, it represents the most significant free-energy change along the $CO_2 \rightarrow HCOO^- \rightarrow HCOOH$ reaction pathway. Therefore, this step governs the overall energetic landscape compared to subsequent hydrogenation steps.

(a) O-TiVC(OH)$_2$

To further explore the reaction pathway of electrochemical CO_2 conversion at the O-TiVC(OH)$_2$ surface, we have carried out a hydrogenation step following CO_2 reduction through the co-adsorption of the formed $HCOO^-$ ion and atomic hydrogen (H). After co-adsorption, the structural relaxation confirms the formation of formic acid (HCOOH) (**Figure 5**), indicating spontaneous and surface-assisted hydrogenation. The calculated energy ΔG of this hydrogenation process is 12.86 kJ/mol (**Table 5**). Various optimized bond lengths and bond angles, along with Bader charge transfer, for the HCOOH molecule are summarized in **Table 5**. The relaxed C-O1, C-O2, C-H1, and O1-H2 bond lengths are 1.36, 1.22, 1.10, and 0.99 Å, respectively, where C-O1 and C-O2 are hydroxyl (C-O) and carbonyl bonds (C=O), respectively. These calculated bond lengths are in good agreement with earlier experimental values: C=O (C-O2) = 1.21 Å, C-O(C-O1) =1.36 Å, C-H1=1.10 Å, and O1-H2=0.97 Å. Similarly, these values demonstrate good consistency with prior theoretical results obtained from a DFT-PBE study, which found theoretical values for these bond lengths of 1.35 Å (C-O1), 1.21 Å (C-O2) Å and 0.97 Å (O1-H2) [43].

PDOS calculations were also performed to gain deeper insights into electronic interactions during the conversion process. The overlapping of p- and s-orbitals of the O and H atoms near the Fermi

level indicated sp-hybridization. It showed strong O-H bond formation between the O atom of $HCOO^-$ and the H atom. Bader charge calculations indicated that during co-adsorption, the formed HCOOH molecule acts as an electron acceptor and becomes negatively charged by gaining a Bader charge of -0.144 e^-.

Table 5

Gibbs free energy ΔG (kJ/mol), bond lengths l(Å), and bond angles θ (°) of HCOOH at -OH functionalized O-TiVC and S-TiVC MXenes.

MXenes	ΔG	Δq	l				θ		
			l_1(C-O1)	l_1(C-O2)	l_3(C-H1)	l_4(O1-H2)	θ_1	θ_2	θ_3
O-TiVC(OH)$_2$	12.86	-0.144	1.36	1.22	1.10	0.99	109.95	125.29	124.75
S-TiVC(OH)$_2$	16.48	0.178	1.40	1.25	1.09	0.98	113.84	124.98	121.13
Experimental [62]	--	--	1.34	1.20	1.09	0.97	111.00	124.10	---
Theoretical [63]	--	--	1.35	1.21	1.09	0.97	--	--	--

(b) S-TiVC(OH)$_2$

Similar to the O-TiVC(OH)$_2$ case, we studied the co-adsorption of HCOO- and H atoms on the S-TiVC(OH)$_2$ surface to elucidate the further conversion of CO_2. As in O-TiVC(OH)$_2$, HCOOH formation also occurs on S-TiVC(OH)$_2$ (**Figure 5**). The Gibbs free energy of this hydrogenation step (at S-TiVC(OH)$_2$) is 3.62 kJ/mol higher than on the O-TiVC(OH)$_2$ surface. Although both configurations of TiVC(OH)$_2$ are thermodynamically feasible, O-TiVC(OH)$_2$ provides a more favorable environment for the hydrogenation of the $HCOO^-$ ion. This minor difference in ΔG implies that adsorption interactions on S-TiVC(OH)$_2$ are less effective in stabilizing the final state (HCOOH), which leads to a marginally higher energy requirement. In contrast to O-TiVC(OH)$_2$, the HCOOH molecule acts as an electron donor and a Bader charge transfer of 0.178e^- takes place between S-TiVC(OH)$_2$ and HCOOH at the surface during the co-adsorption process. Different calculated angles of HCOOH are shown in **Figure 5** and summarized in **Table 5**. Optimized bond angles of HCOOH are θ_1=113.84°, θ_2=124.98°, and θ_3=121.13°, while the bond lengths C-O1, C-O2, C-H1, and O1-H2 are 1.40, 1.25, 1.09, and 0.98 Å, respectively. The schematic of the steps involved in HCOOH formation at the TiVC surface, along with the free energy profile, is shown in **Figure 6**. As is evident from the free-energy profiles, the formation of the $HCOO^-$ intermediate

from CO_2 is thermodynamically favourable for both configurations of $TiVC(OH)_2$. Nevertheless, this step involves CO_2 activation and constitutes the most energetically significant transformation along the $CO_2 \rightarrow HCOO^- \rightarrow$ HCOOH pathway. The subsequent hydrogenation step is comparatively less demanding and proceeds readily once the $HCOO^-$ intermediate is formed. Thus, the overall reaction efficiency and rate are primarily governed by the formate formation step, rather than by the hydrogenation of $HCOO^-$. Once CO_2 is activated at the $TiVC(OH)_2$ surfaces, the reaction proceeds rapidly towards the formation of HCOOH.

In general, the conversion of CO_2 to $HCOO^-$ is considered one of the most energy-demanding steps in CO_2 reduction reactions, as it involves substantial molecular activation and charge transfer. However, in the present system, the calculated free-energy profiles clearly show that on O-$TiVC(OH)_2$ the CO_2 molecule undergoes adsorption-induced activation and spontaneously transforms into a $HCOO^-$ intermediate through hydrogen transfer from a surface -OH group, without encountering an activation barrier. Although this step represents the largest free-energy change relative to subsequent hydrogenation steps, our calculations show it to be thermodynamically favourable. Since no external electrochemical potential is applied in the present DFT framework, assigning a strict potential-determining step (PDS) is not appropriate; instead, the free-energy analysis provides a qualitative description of the relative energetic landscape of the $CO_2 \rightarrow HCOO^- \rightarrow$ HCOOH pathway.

The optimized bond lengths and bond angles of HCOOH adsorbed on the $TiVC(OH)_2$ surface fall within the typical ranges reported for formic acid in previous theoretical and experimental studies. Although most literature values correspond to gas-phase HCOOH, the comparison here is intended to be qualitative, demonstrating that adsorption on the $TiVC(OH)_2$ surface does not lead to significant structural distortion of the HCOOH molecule.

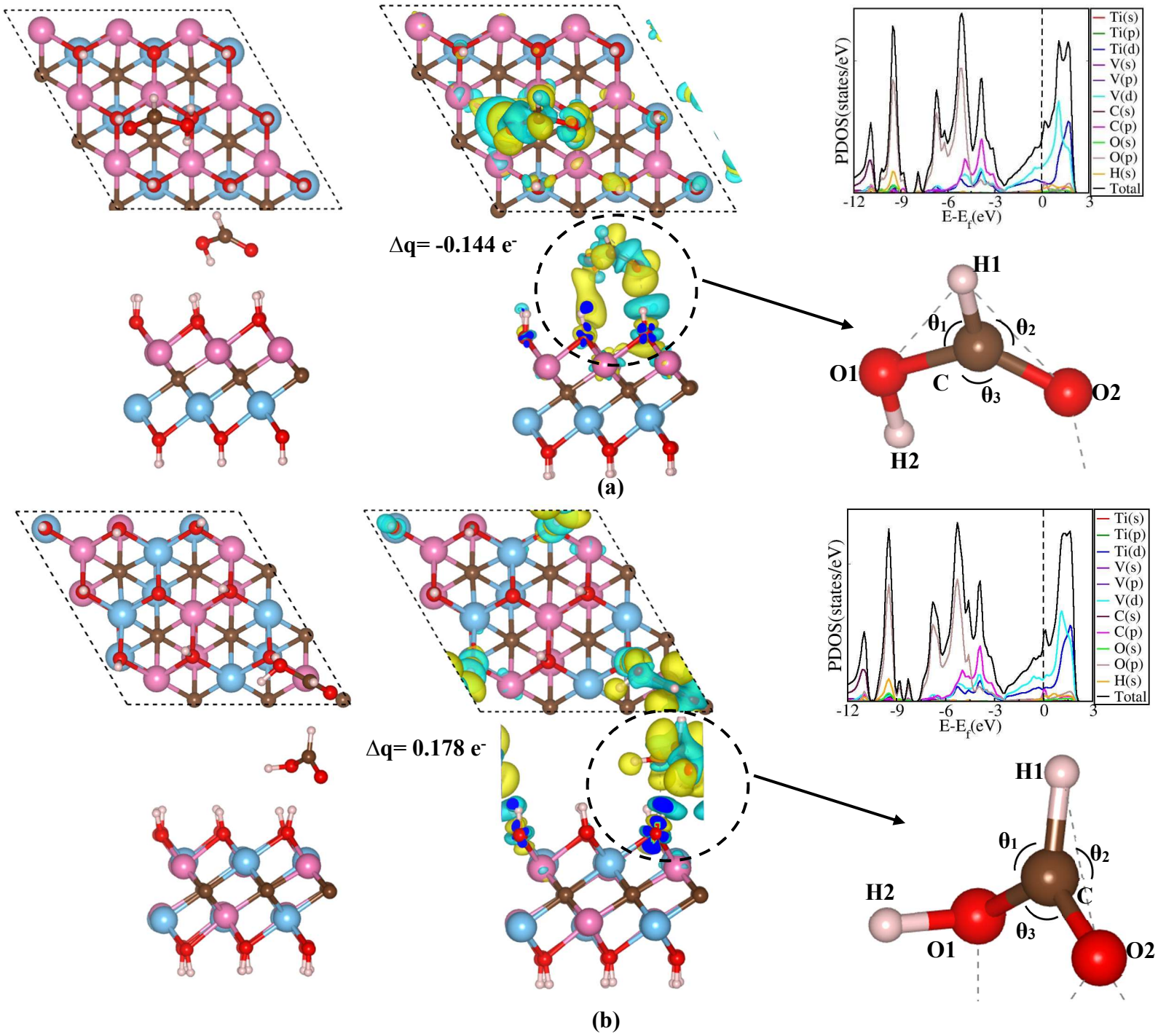

Fig. 5. Relaxed geometries, charge density differences, and PDOS of TiVC after co-adsorption of $HCOO^-$ ion and H atom at (a) O-TiVC$(OH)_2$ and (b) S-TiVC$(OH)_2$ MXenes. In both cases, the formation of formic acid (HCOOH) occurs after the relaxation of the structures.

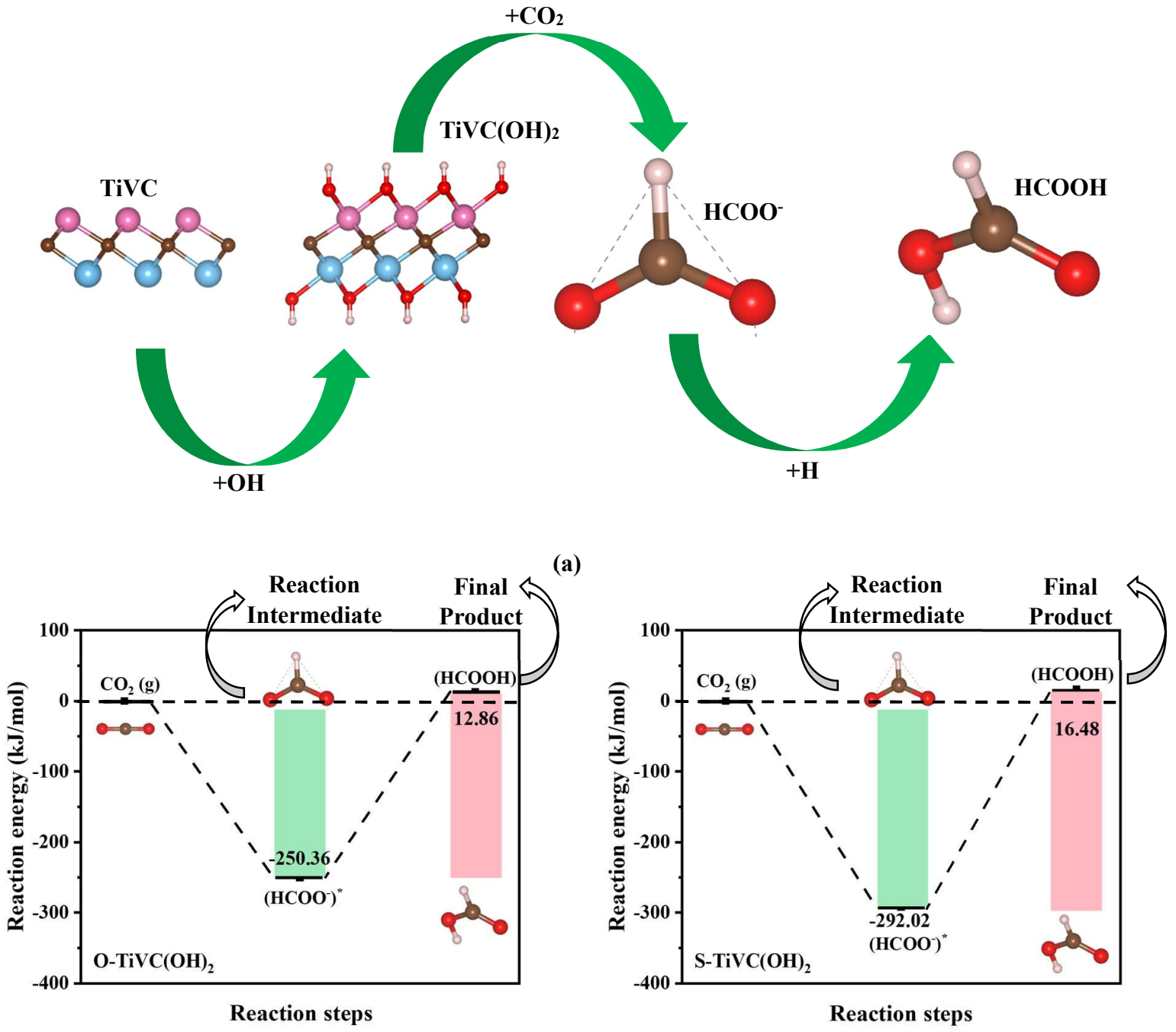

Fig. 6. (a) Illustration of reaction pathway and free energy profile of electrochemical CO_2 conversion at (b) O-TiVC$(OH)_2$ and (c) S-TiVC$(OH)_2$ MXene surfaces. The final product of electrochemical CO_2 conversion at both surfaces is formic acid (HCOOH).

The free-energy profile for the $CO_2 \rightarrow HCOO^- \rightarrow HCOOH$ pathway shows that CO_2 activation to $HCOO^-$ involves the largest free-energy change along the reaction coordinate, whereas the subsequent hydrogenation step is comparatively less demanding. Although no applied electrochemical potential is considered, this indicates that CO_2 activation governs the overall energetic landscape of the reaction rather than the hydrogenation of $HCOO^-$. The CO_2 reduction mechanism is analyzed using Gibbs free-energy diagrams to identify thermodynamically favorable pathways and potential-determining steps, an approach widely adopted in first-principles-based studies. All intermediates are evaluated within a consistent thermodynamic framework, making the relative free-energy trends meaningful for mechanistic comparison. Although activation energy barriers can further provide kinetic insights, their evaluation under electrochemical conditions is beyond the scope of this work. In this work, CO_2 reduction pathways are analyzed within a thermodynamic free-energy framework, which is commonly employed in first-principles-based studies of CO_2 electroreduction. While explicit *H adsorption and HER kinetics can provide additional insight into selectivity, free-energy trends of CO_2RR intermediates are sufficient to identify favorable reaction pathways. The strong thermodynamic stabilization of the $HCOO^-$ intermediate on -OH functionalized TiVC suggests a preferential CO_2RR route. The HER at the same catalyst surfaces and explicit kinetic competition between the two processes will be considered in future studies.

3.6 Benchmarking against state-of-the-art MXene catalysts

Table 6 summarizes the reported free energy changes for CO_2 reduction to formate on various MXene catalysts. Previous studies report ΔG values of approximately -0.28 eV for Ti_2CO_2 and -0.35 eV for $Ti_3C_2(OH)_2$, while Mo_2CO_2 exhibits a stronger thermodynamic driving force of about -0.46 eV toward HCOOH formation. In comparison, OH-functionalized TiVC MXenes show adsorption-induced, barrierless formation of $HCOO^-$ during structural relaxation, driven by direct hydrogen transfer from surface -OH groups. This behavior differs from other systems where protonation requires externally supplied proton-electron pairs. Therefore, beyond comparable thermodynamic stabilization, $TiVC(OH)_2$ demonstrates a distinct surface-assisted activation mechanism, which enhances CO_2 activation and promotes selective formate formation, highlighting its catalytic potential for efficient CO_2 conversion.

Table 6

Comparison of CO_2 to HCOOH performance of TiVC MXenes with reported MXene catalysts based on DFT studies

Materials	Surface Terminations	Key Intermediate	ΔG (*CO_2-*HCOO) (eV)	Ref
O-TiVC	-OH	$HCOO^-$	Spontaneous	--
S-TiVC	-OH	$HCOO^-$	Spontaneous	--
VNbC	-OH	$HCOO^-$	Spontaneous	[64]
V_2C	-OH	$HCOO^-$	Spontaneous	[65]
Ti_3C_2	-OH	$HCOO^-$	-0.35	[66]
Ti_2C	-O	$HCOO^-$	-0.28	[66]
Mo_2C	O	HCOOH	-0.46	[67]

4. Conclusion

We have employed first-principles calculations based on the density functional theory to analyze the interaction of the gaseous CO_2 molecule with TiVC MXenes in both their ordered (O-TiVC) and solid-solution (S-TiVC) phases. We have investigated the pristine surfaces, as well as different functionalized derivatives (O, Cl, F, S, and OH). We observed a wide range of adsorption behaviors, indicating that O-TiVC and S-TiVC MXenes can be utilized as efficient adsorbent materials for CO_2 reduction. The key findings of our study are:

(a) Both TiVC configurations are metallic and preserve this metallic character even after surface functionalization with various functional groups.

(b) Bare O-TiVC and S-TiVC are found to be very reactive towards CO_2 adsorption with maximum adsorption energies of -363.27 kJ/mol and -296.47 kJ/mol, respectively. Furthermore, these MXenes effectively activate CO_2 for its further reduction. In some configurations of CO_2 on pristine S-TiVC, dissociation of the CO_2 molecule takes place, which confirms the higher reactivity of S-TiVC over O-TiVC.

(c) Among all considered TiVC derivatives, -O functionalized O-TiVC and S-TiVC derivatives form the most robust structures with cohesive energies of -8.41 and -8.43 eV, respectively.

(d) Surface functionalization of TiVC alters the activation of CO_2, resulting in weak physical adsorption due to the effect of steric hindrance caused by functionalized surface atoms.

(e) Functionalization of TiVC with the -OH functional group initiates the conversion of CO_2 as the spontaneous formation of a formate ion ($HCOO^-$) takes place at the surface of O-TiVC $(OH)_2$ and S-TiVC $(OH)_2$.

(f) Further co-adsorption of HCOO- and H atoms at the surface of O-TiVC$(OH)_2$ and S-TiVC$(OH)_2$ leads to the formation of formic acid (HCOOH), confirming TiVC$(OH)_2$ as an efficient electrocatalyst for CO_2 conversion.

We emphasize that our computational methodology is based on density functional theory (DFT) calculations in vacuum, typical of thermal catalysis studies. Critical electrochemical factors, such as solvent effects, applied electrode potential, and the structure of the electrochemical double layer, are not explicitly considered in the present work. These factors are essential to evaluate true CO_2RR performance and selectivity under operating conditions and represent important directions for future work. In conclusion, this study shows that surface functionalization critically governs CO_2 activation on TiVC MXenes. Among the considered terminations, -OH functionalization stabilizes the formate ($HCOO^-$) intermediate, revealing an alternative reaction pathway driven by favourable adsorption geometry and electronic structure modulation. While these results highlight the potential of -OH functionalized TiVC MXenes for selective CO_2 conversion to formate, a full assessment of selectivity requires explicit treatment of electrochemical potential, solvation effects, and experimental validation, which will be addressed in future work.

Acknowledgements

AKM acknowledges the Science and Engineering Research Board (SERB) for a state university research excellence (SURE) grant (SUR/2022/004935). Via our membership of the UK's HEC Materials Chemistry Consortium, which is funded by EPSRC (EP/X035859), we acknowledge the use of the ARCHER2 UK National Supercomputing Service (https://www.archer2.ac.uk). This research work was enabled by the financial support provided by UPES, Dehradun, India. We also acknowledge the computational resources of the University of Kassel.

Conflicts of interest: The authors don't have any conflicts of interest.

Data and code availability: Data is available as Supplementary Information.

Supplementary information: We have given the top and side views of O-TiVCT_2 and S-TiVCT_2 MXenes in Figures S1 and S2, while their PDOS are plotted in Figures S3 and S4, respectively.

Figures S5 and S6 contain all studied configurations of CO_2 at O-TiVC and O-TiVCO_2, respectively. Figure S7 consists of the charge density difference of the most stable configurations of CO_2 at O-TiVCT_2. Various configurations of CO_2 at O-TiVCCl_2, O-TiVCF_2, O-TiVCS_2, O-TiV$C(OH)_2$ are shown in Figures S8, S9, S10, S12 respectively. The PDOS of the most stable configurations of CO_2 at O-TiVCT_2 are given in Figure S11. Figures S13-S17 summarize top and side views of different CO_2 configurations at S-TiVC, S-TiVCO_2, S-TiVCF_2, S-TiVCCl_2, and S-TiVCS_2. Figures S18 and S19 contain the PDOS and charge density difference of the most favorable configurations of CO_2 at S-TiVC and S-TiVCT_2. Finally, all studied configurations of CO_2 are plotted in Figure S20.

Ethical approval: Not Applicable.

References

[1] B. Li, N. Haneklaus, The role of renewable energy, fossil fuel consumption, urbanization and economic growth on CO_2 emissions in China, Energy Reports 7 (2021) 783–791. https://doi.org/10.1016/j.egyr.2021.09.194.

[2] S. Dilshad, A.R. Kalair, N. Khan, Review of carbon dioxide (CO_2) based heating and cooling technologies: Past, present, and future outlook, Int. J. Energy Res. 44 (2020) 1408–1463. https://doi.org/10.1002/er.5024.

[3] M. Filonchyk, M.P. Peterson, L. Zhang, V. Hurynovich, Y. He, Greenhouse gases emissions and global climate change: Examining the influence of CO_2, CH_4, and N_2O, Sci. Total Environ. 935 (2024) 173359. https://doi.org/10.1016/j.scitotenv.2024.173359.

[4] N.S. Spinner, J.A. Vega, W.E. Mustain, Recent progress in the electrochemical conversion and utilization of CO_2, Catal. Sci. Technol. 2 (2012) 19–28. https://doi.org/10.1039/C1CY00314C.

[5] S. Overa, B.H. Ko, Y. Zhao, F. Jiao, Electrochemical Approaches for CO_2 Conversion to Chemicals: A Journey toward Practical Applications, Acc. Chem. Res. 55 (2022) 638–648. https://doi.org/10.1021/acs.accounts.1c00674.

[6] K. Kumar, N. H. de Leeuw, J. Adam, A. K. Mishra, Mechanistic insights into CO_2 activation on pristine, vacancy-containing and doped goldene: a single-atom layer of gold. Physical

Chemistry Chemical Physics, 26(2024), 29420-29431. https://doi.org/10.1039/D4CP03087G

[7] K. Kumar, A. Dhasmana, N. de Leeuw, J. Adam, A. K. Mishra, CO_2 activation on metal- and non-metal-doped goldene sheets: A DFT study. Applied Surface Science, (2025) 164509. https://doi.org/10.1016/j.apsusc.2025.164509

[8] K. Kumar, A. Dhasmana, S. Mishra, R. Sharma, N. H. de Leeuw, J. Adam, A. K. Mishra, Defect-mediated CO_2 activation at two-dimensional MgO monolayers: A DFT study. Materials Today Communications, (2025) 112907. https://doi.org/10.1016/j.mtcomm.2025.112907

[9] K. Kumar, A. Dhasmana, N. H. de Leeuw, J. Adam, A. K. Mishra, DFT study of CO_2 activation on pristine and vacancy-containing 2D-GeC monolayers. ChemPhysMater (2025). https://doi.org/10.1016/j.chphma.2025.06.002.

[10] K. Kumar, D. Thakur, R. Sharma, A. K. Mishra, First-principles study of CO_2 activation on pristine and defected XO2 (X= Pd, Pt) monolayers. Journal of Molecular Graphics and Modelling, (2025) 109273. https://doi.org/10.1016/j.jmgm.2025.109273.

[11] G. Wang, J. Chen, Y. Ding, P. Cai, L. Yi, Y. Li, C. Tu, Y. Hou, Z. Wen, L. Dai, Electrocatalysis for CO_2 conversion: from fundamentals to value-added products, Chem. Soc. Rev. 50 (2021) 4993–5061. https://doi.org/10.1039/D0CS00071J.

[12] J. Li, Y. Kuang, Y. Meng, X. Tian, W.-H. Hung, X. Zhang, A. Li, M. Xu, W. Zhou, C.-S. Ku, C.-Y. Chiang, G. Zhu, J. Guo, X. Sun, H. Dai, Electroreduction of CO_2 to Formate on a Copper-Based Electrocatalyst at High Pressures with High Energy Conversion Efficiency, J. Am. Chem. Soc. 142 (2020) 7276–7282. https://doi.org/10.1021/jacs.0c00122.

[13] C. Lu, X. Shi, Y. Liu, H. Xiao, J. Li, X. Chen, Nanomaterials for adsorption and conversion of CO_2 under gentle conditions, Mater. Today 50 (2021) 385–399. https://doi.org/10.1016/j.mattod.2021.03.016.

[14] A.H. Alami, M. Tawalbeh, S. Alasad, M. Ali, M. Alshamsi, H. Aljaghoub, Cultivation of Nannochloropsis algae for simultaneous biomass applications and carbon dioxide capture, Energy Sources, Part A Recover. Util. Environ. Eff. 47 (2025) 8471–8482.

https://doi.org/10.1080/15567036.2021.1933267.

[15] L. Keshavarz, M.R. Ghaani, J.M.D. MacElroy, N.J. English, A comprehensive review on the application of aerogels in CO2-adsorption: Materials and characterisation, Chem. Eng. J. 412 (2021) 128604. https://doi.org/10.1016/j.cej.2021.128604.

[16] H.-Y. Zhuo, X. Zhang, J.-X. Liang, Q. Yu, H. Xiao, J. Li, Theoretical Understandings of Graphene-based Metal Single-Atom Catalysts: Stability and Catalytic Performance, Chem. Rev. 120 (2020) 12315–12341. https://doi.org/10.1021/acs.chemrev.0c00818.

[17] R. Gusmão, M. Veselý, Z. Sofer, Recent Developments on the Single Atom Supported at 2D Materials Beyond Graphene as Catalysts, ACS Catal. 10 (2020) 9634–9648. https://doi.org/10.1021/acscatal.0c02388.

[18] K. Kumar, J. Xu, G. Wu, A. Verma, A. K. Mishra, L. Gao, S. Ogata, Recent Trends and Progress in Molecular Dynamics Simulations of 2D Materials for Tribological Applications: An Extensive Review. Archives of Computational Methods in Engineering, 1-23 (2025). https://doi.org/10.1007/s11831-025-10257-0.

[19] B. Luo, G. Liu, L. Wang, Recent advances in 2D materials for photocatalysis, Nanoscale 8 (2016) 6904–6920. https://doi.org/10.1039/C6NR00546B.

[20] J. Shen, Z. Wu, C. Li, C. Zhang, A. Genest, G. Rupprechter, L. He, Emerging applications of MXene materials in CO_2 photocatalysis, FlatChem 28 (2021) 100252. https://doi.org/10.1016/j.flatc.2021.100252.

[21] J. Ma, Q. Jiang, Y. Zhou, W. Chu, S. Perathoner, C. Jiang, K. Wu, G. Centi, Y. Liu, Tuning the Chemical Properties of Co–Ti 3 C 2 T x MXene Materials for Catalytic CO_2 Reduction, Small 17 (2021). https://doi.org/10.1002/smll.202007509.

[22] J. Ma, Q. Jiang, Y. Zhou, W. Chu, S. Perathoner, C. Jiang, K. Wu, G. Centi, Y. Liu, Tuning the Chemical Properties of Co–Ti 3 C 2 T x MXene Materials for Catalytic CO_2 Reduction, Small 17 (2021). https://doi.org/10.1002/smll.202007509.

[23] A. S. Kharb, K. Kumar, A. K. Chawla, A. K. Mishra, Exploring the gas sensing performances of O-functionalized TiVC MXene: mechanistic insights from computations. Physical Chemistry Chemical Physics, 27(2025), 9041-9055.

https://doi.org/10.1039/D5CP00296F.

[24] A. S. Kharb, K. Kumar, A. K. Chawla, A. K. Mishra, Selective NO gas sensing over TiVCO_2 MXene: A realistic computational prediction. Nano Express, 6(2025), 025009. https://doi.org/10.1088/2632-959X/adda69.

[25] J. Ma, Q. Jiang, Y. Zhou, W. Chu, S. Perathoner, C. Jiang, K. Wu, G. Centi, Y. Liu, Tuning the Chemical Properties of Co–Ti 3 C 2 T x MXene Materials for Catalytic CO_2 Reduction, Small 17 (2021). https://doi.org/10.1002/smll.202007509.

[26] X. Liu, T. Chen, Y. Xue, J. Fan, S. Shen, M.S.A. Hossain, M.A. Amin, L. Pan, X. Xu, Y. Yamauchi, Nanoarchitectonics of MXene/semiconductor heterojunctions toward artificial photosynthesis via photocatalytic CO2 reduction, Coord. Chem. Rev. 459 (2022) 214440. https://doi.org/10.1016/j.ccr.2022.214440.

[27] J. Heo, N. Her, M. Jang, C.M. Park, A. Son, J. Han, Y. Yoon, Photocatalytic and electrocatalytic reduction of CO 2 by MXene-based nanomaterials: A review, Crit. Rev. Environ. Sci. Technol. 53 (2023) 987–1008. https://doi.org/10.1080/10643389.2022.2101857.

[28] F.-Q. Liu, X. Liu, L. Sun, R. Li, C.-X. Yin, B. Wu, MXene-supported stable adsorbents for superior CO_2 capture, J. Mater. Chem. A 9 (2021) 12763–12771. https://doi.org/10.1039/D1TA01403J.

[29] M. Aliyu, B.O. Yusuf, A.S. Abdullahi, A.I. Bakare, M. Umar, A.S. Hakeem, S.A. Ganiyu, Ti_2C-MXene/activated carbon nanocomposite for efficient CO_2 capture: Insights into thermodynamics properties, Sep. Purif. Technol. 340 (2024) 126737. https://doi.org/10.1016/j.seppur.2024.126737.

[30] Z. Hu, Y. Xie, D. Yu, Q. Liu, L. Zhou, K. Zhang, P. Li, F. Hu, L. Li, S. Chou, S. Peng, Hierarchical Ti 3 C 2 T x MXene/Carbon Nanotubes for Low Overpotential and Long-Life Li-CO 2 Batteries, ACS Nano 15 (2021) 8407–8417. https://doi.org/10.1021/acsnano.0c10558.

[31] Z. Hu, Y. Xie, D. Yu, Q. Liu, L. Zhou, K. Zhang, P. Li, F. Hu, L. Li, S. Chou, S. Peng, Hierarchical $Ti_3C_2T_x$ MXene/Carbon Nanotubes for Low Overpotential and Long-Life Li-

CO_2 Batteries, ACS Nano 15 (2021) 8407–8417. https://doi.org/10.1021/acsnano.0c10558.

[32] G. Murali, J.K. Reddy Modigunta, Y.H. Park, J.-H. Lee, J. Rawal, S.-Y. Lee, I. In, S.-J. Park, A Review on MXene Synthesis, Stability, and Photocatalytic Applications, ACS Nano 16 (2022) 13370–13429. https://doi.org/10.1021/acsnano.2c04750.

[33] S. Mehdi Aghaei, A. Aasi, B. Panchapakesan, Experimental and Theoretical Advances in MXene-Based Gas Sensors, ACS Omega 6 (2021) 2450–2461. https://doi.org/10.1021/acsomega.0c05766.

[34] Á. Morales-García, F. Calle-Vallejo, F. Illas, MXenes: New Horizons in Catalysis, ACS Catal. 10 (2020) 13487–13503. https://doi.org/10.1021/acscatal.0c03106.

[35] X. Li, Z. Huang, C.E. Shuck, G. Liang, Y. Gogotsi, C. Zhi, MXene chemistry, electrochemistry and energy storage applications, Nat. Rev. Chem. 6 (2022) 389–404. https://doi.org/10.1038/s41570-022-00384-8.

[36] X. Li, Z. Huang, C.E. Shuck, G. Liang, Y. Gogotsi, C. Zhi, MXene chemistry, electrochemistry and energy storage applications, Nat. Rev. Chem. 6 (2022) 389–404. https://doi.org/10.1038/s41570-022-00384-8.

[37] K.R.G. Lim, M. Shekhirev, B.C. Wyatt, B. Anasori, Y. Gogotsi, Z.W. Seh, Fundamentals of MXene synthesis, Nat. Synth. 1 (2022) 601–614. https://doi.org/10.1038/s44160-022-00104-6.

[39] K. Huang, P. Qu, Y. Wang, C. Lian, J. Li, H. Su, H. Liu, Mechanistic Insights for the Electrocatalytic CO_2 Reduction on M_2C-Type MXenes, Ind. Eng. Chem. Res. 62 (2023) 20716–20726. https://doi.org/10.1021/acs.iecr.3c02962.

[40] Z. Guo, Y. Li, B. Sa, Y. Fang, J. Lin, Y. Huang, C. Tang, J. Zhou, N. Miao, Z. Sun, M2C-type MXenes: Promising catalysts for CO2 capture and reduction, Appl. Surf. Sci. 521 (2020) 146436. https://doi.org/10.1016/j.apsusc.2020.146436.

[41] B. Ding, W.-J. Ong, J. Jiang, X. Chen, N. Li, Uncovering the electrochemical mechanisms for hydrogen evolution reaction of heteroatom doped M_2C MXene (M = Ti, Mo), Appl. Surf. Sci. 500 (2020) 143987. https://doi.org/10.1016/j.apsusc.2019.143987.

[42] X. Zhang, Z. Zhang, J. Li, X. Zhao, D. Wu, Z. Zhou, Ti_2CO_2 MXene: a highly active and selective photocatalyst for CO_2 reduction, J. Mater. Chem. A 5 (2017) 12899–12903. https://doi.org/10.1039/C7TA03557H.

[43] A. Junkaew, R. Arroyave, Enhancement of the selectivity of MXenes (M2C, M= Ti, V, Nb, Mo) via oxygen-functionalization: promising materials for gas-sensing and-separation. Physical Chemistry Chemical Physics, 20(2018), 6073-6082. https://doi.org/10.1039/C7CP08622A.

[44] A. Jurado, K. Ibarra, A. Morales-García, F. Viñes, F. Illas, Adsorption and activation of CO_2 on nitride MXenes: composition, temperature, and pressure effects. ChemPhysChem, 22(2021), 2456-2463. https://doi.org/10.1002/cphc.202100600.

[45] R. Morales-Salvador, J. D. Gouveia, A. Morales-Garcia, F. Vines, J. R. Gomes, F. Illas, Carbon capture and usage by MXenes. ACS Catalysis, 11(2021), 11248-11255. https://doi.org/10.1021/acscatal.1c02663.

[46] R. Morales-Salvador, A. Morales-Garcia, F. Vines, F. Illas, Two-dimensional nitrides as highly efficient potential candidates for CO_2 capture and activation. Physical Chemistry Chemical Physics, 20(2018), 17117-17124. https://doi.org/10.1039/C8CP02746C.

[47] J. Yang, L. Sun, Z. He, W. Xu, J. Peng, First-principles computational screening of CO_2 gas adsorption by two-dimensional transition metals M2N-MXene. *Journal of Materials Science*, (2025)1-18. https://doi.org/10.1007/s10853-025-10721-z

[48] S. Yazdanparast, S. Soltanmohammad, A. Fash-White, G.J. Tucker, G.L. Brennecka, Synthesis and Surface Chemistry of 2D TiVC Solid-Solution MXenes, ACS Appl. Mater. Interfaces 12 (2020) 20129–20137. https://doi.org/10.1021/acsami.0c03181.

[49] S. P. Huang, J. Zhang, Y.-R. Ren, W.-K. Chen, Investigating the potentials of TiVC MXenes as anode materials for Li-ion batteries by DFT calculations, Appl. Surf. Sci. 569 (2021) 151002. https://doi.org/10.1016/j.apsusc.2021.151002.

[50] P. Giannozzi, O. Andreussi, T. Brumme, O. Bunau, M. Buongiorno Nardelli, M. Calandra, R. Car, C. Cavazzoni, D. Ceresoli, M. Cococcioni, N. Colonna, I. Carnimeo, A. Dal Corso, S. de Gironcoli, P. Delugas, R.A. DiStasio, A. Ferretti, A. Floris, G. Fratesi, G. Fugallo, R.

Gebauer, U. Gerstmann, F. Giustino, T. Gorni, J. Jia, M. Kawamura, H.-Y. Ko, A. Kokalj, E. Küçükbenli, M. Lazzeri, M. Marsili, N. Marzari, F. Mauri, N.L. Nguyen, H.-V. Nguyen, A. Otero-de-la-Roza, L. Paulatto, S. Poncé, D. Rocca, R. Sabatini, B. Santra, M. Schlipf, A.P. Seitsonen, A. Smogunov, I. Timrov, T. Thonhauser, P. Umari, N. Vast, X. Wu, S. Baroni, Advanced capabilities for materials modelling with Quantum ESPRESSO, J. Phys. Condens. Matter 29 (2017) 465901. https://doi.org/10.1088/1361-648X/aa8f79.

[51] M. Orio, D.A. Pantazis, F. Neese, Density functional theory, Photosynth. Res. 102 (2009) 443–453. https://doi.org/10.1007/s11120-009-9404-8.

[52] J.P. Perdew, K. Burke, M. Ernzerhof, Generalized Gradient Approximation Made Simple, Phys. Rev. Lett. 77 (1996) 3865–3868. https://doi.org/10.1103/PhysRevLett.77.3865.

[53] M. Ropo, K. Kokko, L. Vitos, Assessing the Perdew-Burke-Ernzerhof exchange-correlation density functional revised for metallic bulk and surface systems, Phys. Rev. B 77 (2008) 195445. https://doi.org/10.1103/PhysRevB.77.195445.

[54] G. Kresse, D. Joubert, From ultrasoft pseudopotentials to the projector augmented-wave method, Phys. Rev. B 59 (1999) 1758–1775. https://doi.org/10.1103/PhysRevB.59.1758.

[55] J. Moellmann, S. Grimme, DFT-D3 Study of Some Molecular Crystals, J. Phys. Chem. C 118 (2014) 7615–7621. https://doi.org/10.1021/jp501237c.

[56] H. Zhu, N. Qiu, G. Fang, S. Du, First-principles study on the structure and electronic properties of M 2 CS x (M= Sc, Ti, Y, Zr and Hf, x= 1, 2). RSC advances, 13(2023), 21690-21702. https://doi.org/10.1039/D3RA03340F.

[57] D. Ontiveros, F. Viñes, C. Sousa, Exploring the photoactive properties of promising MXenes for water splitting. Journal of Materials Chemistry A, 13(2025), 3302-3316. https://doi.org/10.1039/D4TA06852A

[58] A. Vig, E. Doan, K. Yang, First-principles investigation of size effects on cohesive energies of transition-metal nanoclusters. Nanomaterials, 13(2023), 2356. https://doi.org/10.3390/nano13162356.

[59] S. Thevuthasan, G. Herman, Y. Kim, S. Chambers, C.H. Peden, Z. Wang, R. Ynzunza, E. Tober, J. Morais, C.. Fadley, The structure of formate on TiO2(110) by scanned-energy

and scanned-angle photoelectron diffraction, Surf. Sci. 401 (1998) 261–268. https://doi.org/10.1016/S0039-6028(97)01092-3.

[60] M.A. Brown, F. Vila, M. Sterrer, S. Thürmer, B. Winter, M. Ammann, J.J. Rehr, J.A. van Bokhoven, Electronic Structures of Formic Acid (HCOOH) and Formate (HCOO –) in Aqueous Solutions, J. Phys. Chem. Lett. 3 (2012) 1754–1759. https://doi.org/10.1021/jz300510r.

[61] J. D. Gouveia, J. R. B. Gomes, Effect of the surface termination on the adsorption of flue gas by the titanium carbide MXene. Materials Today Chemistry, 29(2023), 101441. https://doi.org/10.1016/j.mtchem.2023.101441.

[62] J. Park, D.E. Woon, Theoretical Modeling of Formic Acid (HCOOH), Formate (HCOO–), and Ammonium (NH4+) Vibrational Spectra in Astrophysical Ices, Astrophys. J. 648 (2006) 1285–1290. https://doi.org/10.1086/506175.

[63] W.W. Rudolph, G. Irmer, Raman Spectroscopic Studies on Aqueous Sodium Formate Solutions and DFT Calculations, J. Solution Chem. 51 (2022) 935–961. https://doi.org/10.1007/s10953-022-01170-2.

[64] D. Thakur, K. Kumar, A. Gupta, A. K. Mishra, Mechanistic insights into CO_2 reduction on pristine and functionalized VNbC MXenes. Discover Materials (2026). https://doi.org/10.1007/s43939-026-00536-3

[65] A. Kajal, K. Kumar, A. S. Kharb, A. K. Mishra, Surface chemistry–driven CO_2 activation conversion on V_2C MXenes. Scientific Reports, 15(2025), 38384. https://doi.org/10.1038/s41598-025-22339-x

[66] C. Y. J. Lim, A. D. Handoko, Z. W. Seh, A realistic take on MXenes for electrochemical reduction of carbon dioxide. Diamond and Related Materials, 130(2022), 109461. https://doi.org/10.1016/j.diamond.2022.109461.

[67] A. D. Handoko, K. D., Fredrickson, B. Anasori, K. W. Convey, L. R. Johnson, Y. Gogotsi, Z. W. Seh, Tuning the basal plane functionalization of two-dimensional metal carbides (MXenes) to control hydrogen evolution activity. ACS Applied Energy Materials, 1(2017), 173-180. https://doi.org/10.1021/acsaem.7b00054.